

USING PRESENCE OF CALCITE CAP ROCK  
IN SHALES TO PREDICT OCCURRENCE OF RESERVOIRS  
COMPOSED OF LEACHED SECONDARY POROSITY  
IN THE GEOPRESSURED ZONE:

Annual Report For The Period

June 1, 1980 - October 31, 1980

by

W. R. Kaiser, Kinji Magara,  
K. L. Milliken, and D. L. Richmann

Bureau of Economic Geology  
W. L. Fisher, Director  
The University of Texas at Austin  
University Station, Box X  
Austin, Texas 78712

Prepared for

U.S. Department of Energy  
Nevada Operations Office  
Las Vegas, Nevada

Work performed under contract

DE-AC08-79ET27111

January, 1981

## Contents

	Page
Abstract . . . . .	1
Introduction . . . . .	1
Cap Rock Mapping . . . . .	2
Fluid Flow Mapping . . . . .	3
Cap Rock Petrology . . . . .	8
Background . . . . .	8
Sampling and Analytical Techniques . . . . .	9
Preliminary Results . . . . .	9
Isotope Chemistry . . . . .	14
Detrital Feldspar Composition . . . . .	18
Background . . . . .	18
Sampling and Analytical Techniques . . . . .	19
Preliminary Results . . . . .	20
Estimating Thermodynamic Functions . . . . .	23
Ca-Montmorillonite . . . . .	27
Ferroan Calcite . . . . .	29
Acknowledgments . . . . .	30
References . . . . .	31

## Figures

1. Distribution by county of organic carbon content of shales in the Frio Formation study area and adjacent areas . . . . .	4
2. Histogram of organic carbon content in the Frio Formation . . . . .	5
3. Schematic diagrams showing shale porosity or transit time versus depth and fluid pressure versus depth relationships . . . . .	6
4. Schematic cross section showing interpreted directions of present fluid flow . . . . .	7

	Page
5. Foraminifers, GCO/DOE No. 2 Pleasant Bayou . . . . .	11
6. Coccolithophores, Humble No. 1 Vieman . . . . .	11
7. Detailed views of foraminifers, Humble No. 1 Skrabanek . . . . .	12
8. Close examination of coccoliths, GCO/DOE No. 2 Pleasant Bayou . . . . .	12
9a. Single rhomb (Fe-bearing carbonate), GCO/DOE No. 2 Pleasant Bayou . . . . .	13
9b. Cluster of rhombs, GCO/DOE No. 2 Pleasant Bayou . . . . .	13
10. Calcite peaks height from X-ray diffractometer traces versus depth, Brazoria County shales . . . . .	15
11. Bulk carbonate oxygen and carbon isotopic data versus depth, Brazoria County shales . . . . .	16
12. Distribution of detrital feldspar compositions, Miocene . . . . .	21
13. Distribution of detrital feldspar compositions, Frio . . . . .	22
14. Estimation of the standard change in enthalpy of formation of phyllosilicates . . . . .	28

Tables

1. Brazoria County isotope data . . . . .	17
2. Compositions of key minerals . . . . .	24
3. Hydrolysis reactions . . . . .	25
4. Reaction pairs . . . . .	26

## ABSTRACT

The distribution of high-resistivity shale in the Frio Formation between hydro pressured and geopressed strata has been mapped along the Texas Gulf Coast. Two high-resistivity intervals more than 1,000 ft thick have been mapped, one in Brazoria and Galveston Counties and the other in Kenedy County. They coincide with Frio delta systems and may be related to extraordinary quantities of CO<sub>2</sub> produced by deltaic sediments rich in woody and herbaceous matter. Beyond being calcareous, the nature of the high-resistivity interval is enigmatic and its relationship to deep secondary porosity problematic. Most of the contained carbonate is microscopically and isotopically skeletal in origin, revealing no evidence of diagenetic modification. Minor rhombs of iron-bearing carbonate tens of microns in size were identified. Detrital feldspar compositions are being established to test subsequent changes in feldspar composition resulting from progressive burial and albitization. Hydrolysis reactions for authigenic minerals and reactions between key pairs of minerals have been written. Thermodynamic functions for complex phyllosilicates at temperatures up to 200°C have been calculated. From thermodynamic calculations it was predicted that ferroan calcite would be the favored authigenic carbonate in shales.

## INTRODUCTION

Two areas of cap rock occurrence have been mapped, one in the upper Texas coast and the other in South Texas. These may be related to ancient delta systems. Two high-resistivity zones have been identified in Brazoria County. The nature of the high-resistivity intervals remains enigmatic. Most of the

carbonate they contain is microscopically and isotopically skeletal in origin. Few authigenic components have been identified. Isotopic data suggest minimal recycling of pore waters between shale and sandstone.

Hydrolysis reactions and reactions between key pairs of minerals have been written. The goal is to plot formation waters on stability diagrams for these reaction pairs and to correlate log activity ratios with the presence or absence of cap rock and deep secondary porosity. Mineral compositions are determined on the basis of microprobe data from earlier Sandstone Consolidation projects and new data collected in this project. Methods have been developed to estimate thermodynamic functions for most of these minerals at elevated temperatures. Methods differ depending on the mineral class and availability of published thermodynamic data.

#### CAP ROCK MAPPING

Cross sections and maps of the shale cap rock (high-resistivity zones) have been made from several hundred geophysical logs. Two main areas of cap rock have been mapped, one in Brazoria and Galveston Counties and the other in Kenedy County. In Brazoria County two high-resistivity zones at 7,000 to 8,000 ft and 10,000 to 12,000 ft have been identified. The shallower zone is at the base of the hydro pressured interval (0.465 psi/ft), and the deeper one is near the boundary between the soft geopressed and hard geopressed intervals (0.7 psi/ft). The deeper zone is regionally more extensive than the shallower zone.

Geographically, the cap rock appears to coincide with two Frio delta systems, the Houston delta system on the upper coast and the Norias delta system in South Texas. It is further suggested that since delta sediments are

normally rich in woody and herbaceous organic matter, an extraordinary quantity of CO<sub>2</sub> is produced in these areas, contributing to cap rock formation. In contrast, interdeltatic areas seem to have no major cap rock development, and its absence is believed to be related to a greater abundance of amorphous organic matter.

Data on the percentage of organic carbon have been compiled for the Frio Formation (fig. 1). A histogram shows that most samples range from about 0.1 to 0.4 weight percent and average 0.28 weight percent (fig. 2). The commonly accepted lower limit for significant oil generation in other basins is approximately 0.5 percent.

#### FLUID FLOW MAPPING

Using digital sonic log data, we plan to map the current vertical and horizontal compaction fluid-flow patterns in Brazoria County. Sonic transit time can be related to porosity or compaction level of shale. Because of a close relation among the level of shale compaction, depth of burial, and pore-fluid pressure, it is possible to estimate the pore-fluid pressure at a given depth from the level of shale compaction or shale transit time value (fig. 3). The estimated pore-fluid pressure values in shales may be used to interpret the vertical and horizontal fluid-flow patterns that currently exist in the subsurface (fig. 4).

However, fluid-flow patterns in the geologic past are probably different from the present patterns. This is because the paleo fluid flow is controlled mainly by the loading patterns and by the fluid-expulsion efficiency of the sedimentary sequences. Whether or not a given sedimentary sequence retained relatively high efficiency for fluid expulsion in the geological past can be

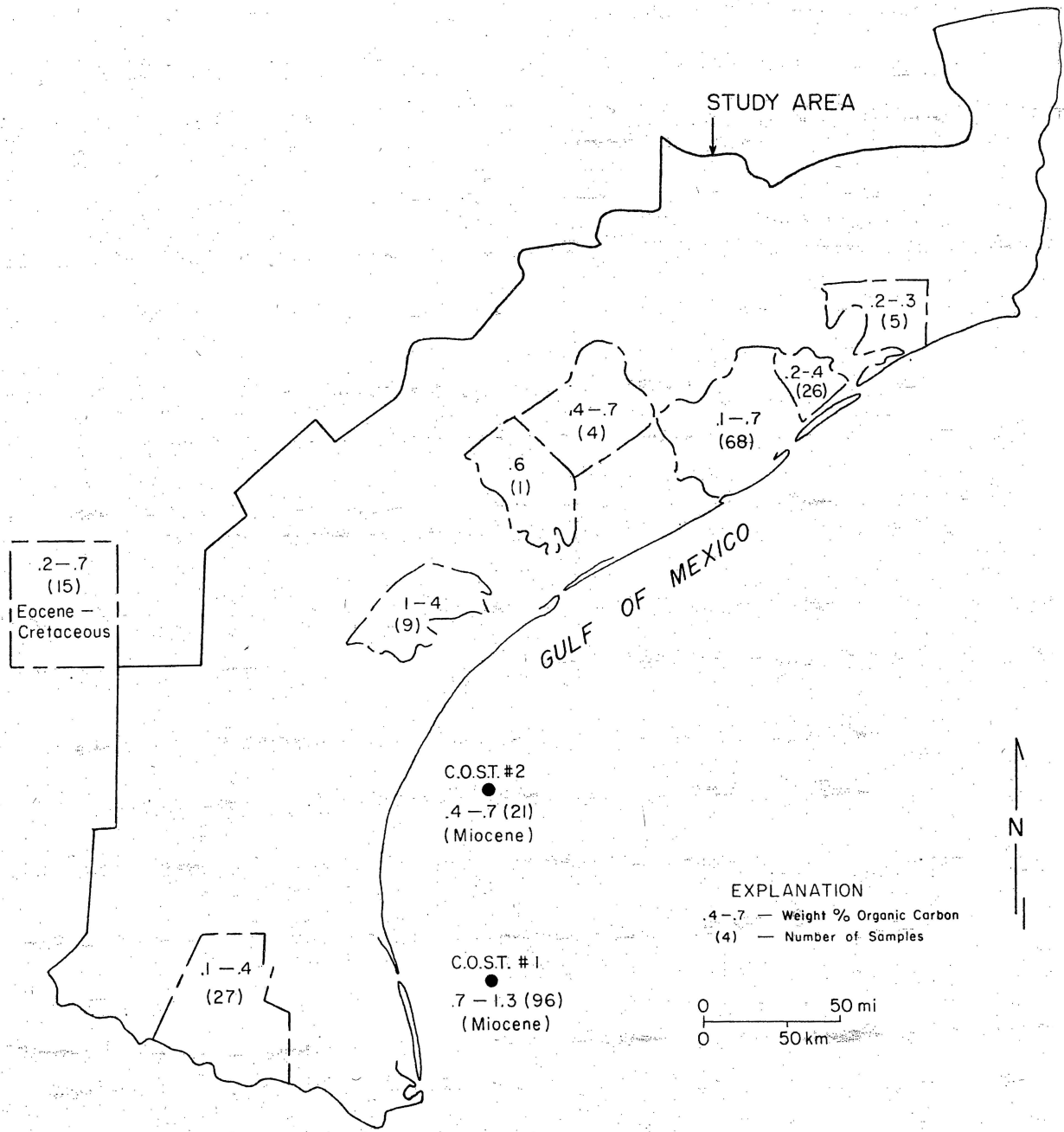


Figure 1. Distribution by county of organic carbon content of shales in the Frio Formation study area and adjacent areas.

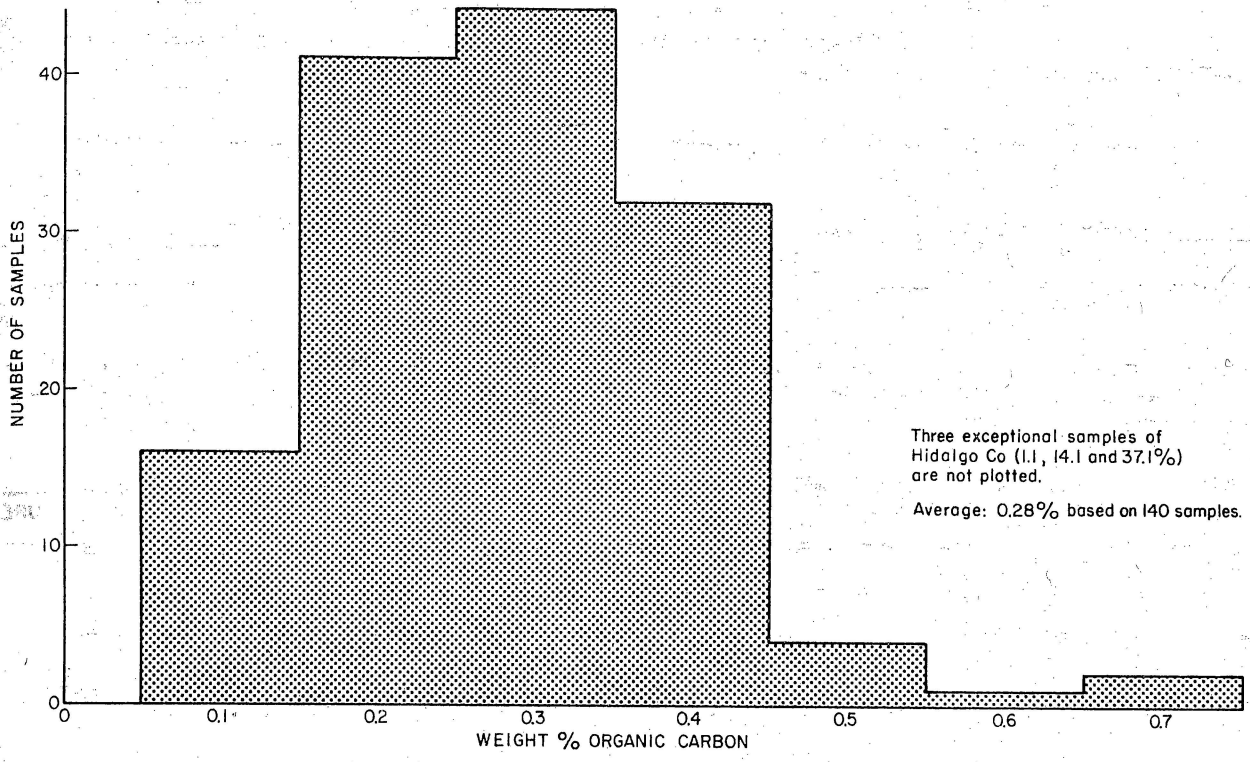


Figure 2. Histogram of organic carbon content in the Frio Formation.



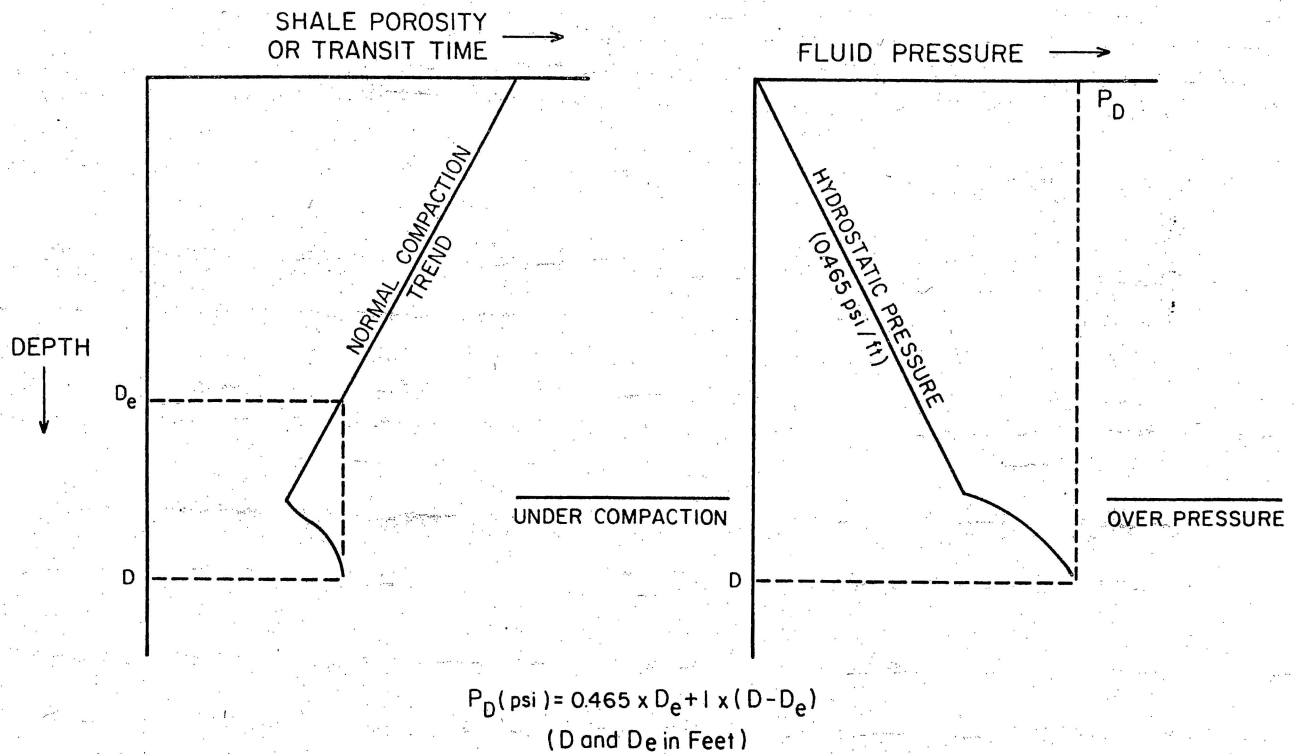


Figure 3. Schematic diagrams showing shale porosity or transit time versus depth and fluid pressure versus depth relationships. Equation is for calculating fluid pressure at depth D in an undercompacted interval.

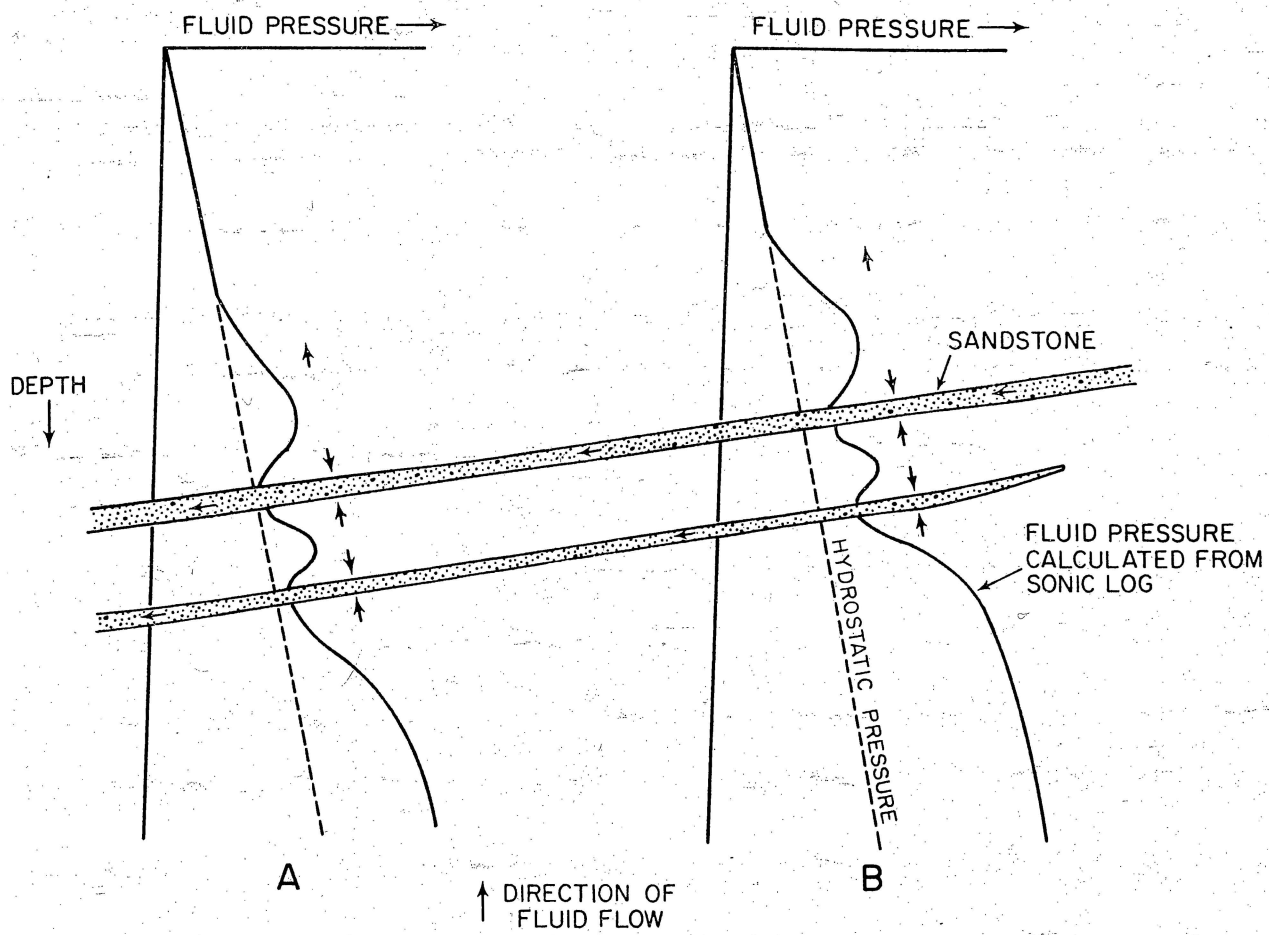


Figure 4. Schematic cross section showing interpreted directions of present fluid flow using fluid-pressure profiles derived from sonic logs. Excess pressure at B, therefore fluid flow from right to left in sandstone.

evaluated by the comparison of the sediment's total load pressure and of the remaining pore-fluid pressure. If most of the load pressure was relieved owing to effective fluid expulsion, it would now have relatively low pressure. Such a sedimentary unit would indicate very little movement of fluids now, but significant fluid expulsion and movement in the geologic past. The objective of the paleo and present fluid-flow analyses is to indicate the direction of movement of fluids containing mineral solutes and to infer the likely places for precipitation of minerals.

In summary, the paleo and the present fluid-flow patterns must be analyzed separately. For the paleo fluid-flow study, a loading map (map showing the total weight of sedimentary column) can be constructed and used. For the present fluid-flow study, the pressure values derived from the analysis of sonic transit time can be used.

## CAP ROCK PETROLOGY

### Background

Heretofore, no one has conducted detailed petrographic analyses of cap rock or high-resistivity shale to explain its response on geophysical logs; that is, why do shale resistivities within these intervals increase so abruptly? Is this effect related to shale mineralogy, pore fluids, or some other feature of the rock?

It is known that cap rock is calcareous, but the nature of the carbonate material has never been documented. One of the major objectives of this study is to determine the genetic association of these carbonates. If they prove to be authigenic and if it can be shown that high resistivity is related to their presence, then the distribution of cap rock, cemented with material possibly

leached from the underlying strata, could bear some relationship to deep secondary porosity. On the other hand, if resistivity cannot be related to the presence of authigenic carbonate (or other authigenic minerals) some other physical or chemical parameter must control it.

### Sampling and Analytical Techniques

On the basis of shale resistivity and interval transit time plots, cap rock intervals were identified in three wells from Brazoria County: GCO/DOE No. 2 Pleasant Bayou, Humble No. 1 J. M. Skrabanek, and Humble No. 1 R. W. Vieman. In all three wells, a shallow and a deeper high-resistivity cap rock zone was identified. Whole-core samples from the intervals of interest were not available; however, we obtained washed cuttings from these wells over portions of each cap rock interval and from the section above and below these intervals. From the washed cuttings, a pure shale sample of about 5 grams was hand picked under the binocular microscope. These shale cuttings were examined on the scanning electron microscope (SEM) as whole rock fragments and in ultrasonically disaggregated size fractions. In addition, disaggregated samples in liquid mounts were examined with a standard polarizing microscope.

The sole petrographic criterion we used to identify authigenic minerals was crystal morphology. By analogy to coarser grained sediments, authigenic phases typically develop euhedral crystal faces where they grow into pore spaces. Thus, we would expect that authigenic carbonates present in the shales might occur as recognizable rhombs.

### Preliminary Results

Identification of individual constituents of the cap rock is best accomplished using disaggregated samples. In the whole cuttings, many of the

constituents were impossible to identify without the energy dispersive analyzer (EDA) because of dense coatings of detrital clay that obscured their morphology. This problem was largely alleviated by using the disaggregated samples.

Disaggregated samples were examined in the following size fractions:  $<2\mu\text{m}$ ; 2 to  $20\mu\text{m}$ ;  $>20\mu\text{m}$ ; and whole sample. Most of our data were obtained from observations of the  $>20\mu\text{m}$ - and 2- to  $20\mu\text{m}$ -size fractions. In these splits, we found that skeletal carbonate, consisting of coccolith and foraminifer fragments, composes a significant portion of the sample (figs. 5 and 6). In fact, in the shallow cap rock zones of all three wells, it is the only form of carbonate that could be positively identified by SEM. The detailed structures of the foraminifers and coccoliths are remarkably well preserved. High-magnification views of these features (figs. 7 and 8) fail to reveal any evidence of diagenetic modification.

Under the petrographic microscope, some micritic fragments were also observed; these may represent the lithified product of carbonate mud present upon deposition. However, these fragments are volumetrically less abundant than fossils.

In some samples from the deeper cap rock zones in each of the three wells, minor quantities of a rhombic mineral were observed (figs. 9a and 9b). These rhombs are iron-bearing carbonate. In all instances that the rhombic carbonates were observed, they occur in extremely minor quantities and are far less abundant than the skeletal carbonate. Also, there are problems in interpreting the genesis of these carbonates on the basis of their form alone. First, they are too large to have formed as a pore-filling cement. Most are tens of microns across and thus probably did not form in micropores (on the order of  $0.1\mu\text{m}$ ) between the clay flakes of a compacted shale. This does not, however, exclude the possibility that they may have formed authigenically

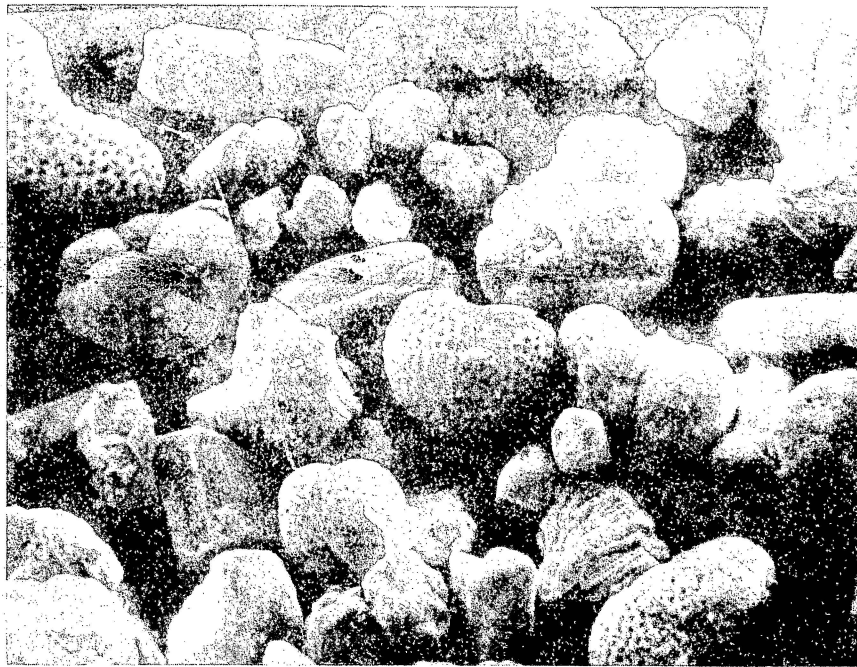


Figure 5. Foraminifers. Foraminiferal tests constitute a significant part of the  $> 20 \mu\text{m}$  fraction; 9,260 to 9,290 ft, GCO/DOE No. 2 Pleasant Bayou.



Figure 6. Coccolithophores. Coccoliths, often in the form of entire coccospheres, are abundant in the 2 to  $20 \mu\text{m}$  fraction; 9,716 ft; Humble No. 1 Vieman; 3,700x.

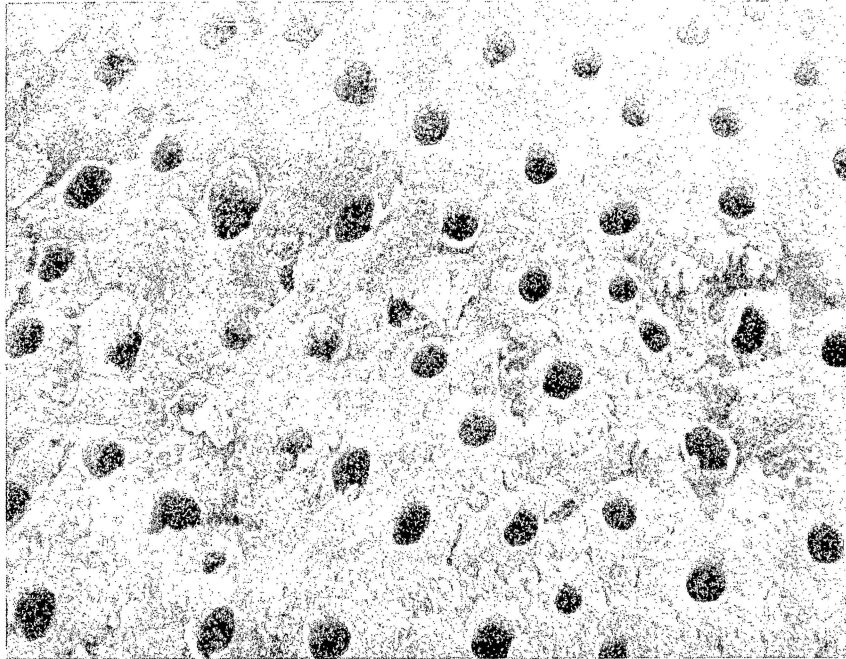


Figure 7. Detailed views of foraminifera reveal no evidence of dissolution or precipitation of authigenic minerals in pores; 6,937 ft; Humble No. 1 Skrabanek; 5,100x.

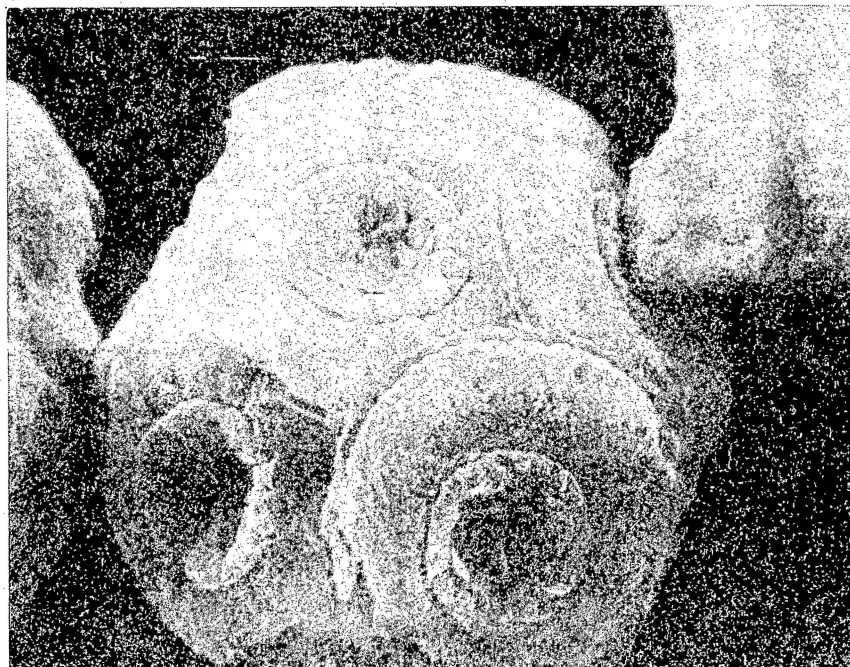


Figure 8. Close examination of coccoliths also reveals little evidence of textural modification from diagenesis; 10,010 ft; GCO/DOE No. 2 Pleasant Bayou; 4,900x.

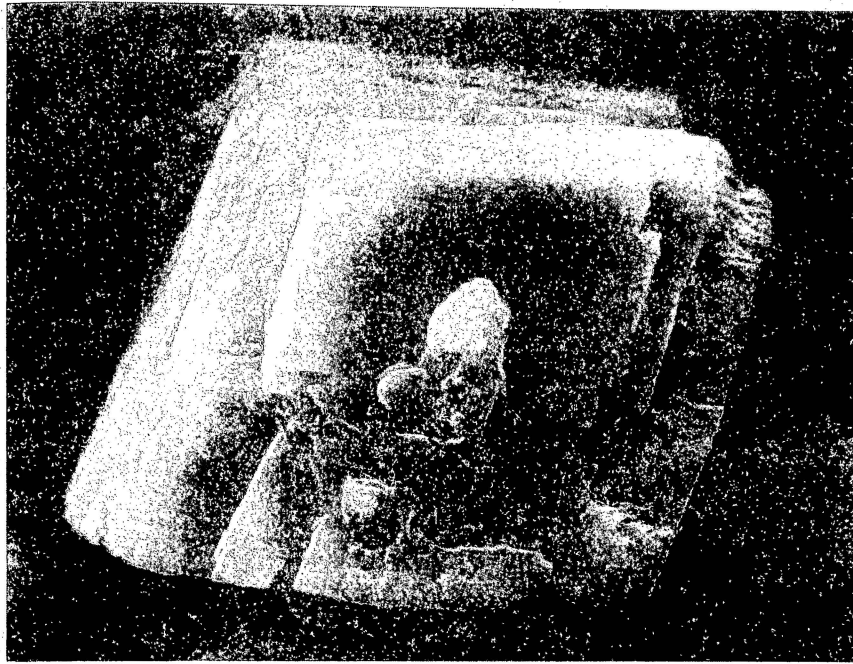


Figure 9a. Single rhomb (Fe-bearing carbonate); 10,010 ft; GCO/DOE No. 2 Pleasant Bayou; 3,200x.



Figure 9b. Cluster of rhombs; 10,010 ft, GCO/DOE No. 2 Pleasant Bayou; 5,200x.



within fractures, as an alteration of detrital material, or within foraminifer chambers. The only clearly authigenic mineral that we have found to occur abundantly in the coarse fractions of the shales is pyrite occurring as framboids.

It is interesting that the consolidation state of the shale does not appear to differ between cap rock and non-cap rock intervals. All samples shallower than 13,000 ft are virtually unlithified and disaggregate spontaneously on contact with water. Below this depth, lithification proceeds rapidly with increasing depth to form very hard, splintery, slate-like shales. The transition to lithified shale roughly corresponds to the total loss of carbonate with depth (fig. 10) and the stabilization of mixed-layer illite/smectite at approximately 80 percent illite layers (Freed, 1980). Intergrowth of clay flakes may be responsible for the increasing lithification.

#### ISOTOPE GEOCHEMISTRY

Twenty-two shale samples from the same three wells in the Chocolate Bayou Field have been analyzed for oxygen and carbon isotopes. To obtain CO<sub>2</sub> gas for isotopic analysis, carbonate in the bulk shale sample is reacted under vacuum with 100 percent anhydrous phosphoric acid. Shale samples for isotopic analysis are selectively removed by hand from cuttings, ground in a ceramic mortar, and X-rayed to determine the number of carbonate phases present and their relative abundance. All Brazoria County samples examined so far are calcite.

Isotopic data obtained so far are consistent with a carbonate fraction consisting primarily of skeletal debris (fig. 11; table 1). At all depths examined,  $\delta^{18}\text{O}$  values for carbonates in shales are significantly heavier than the  $\delta^{18}\text{O}$  values for carbonates in associated sandstones (Loucks and

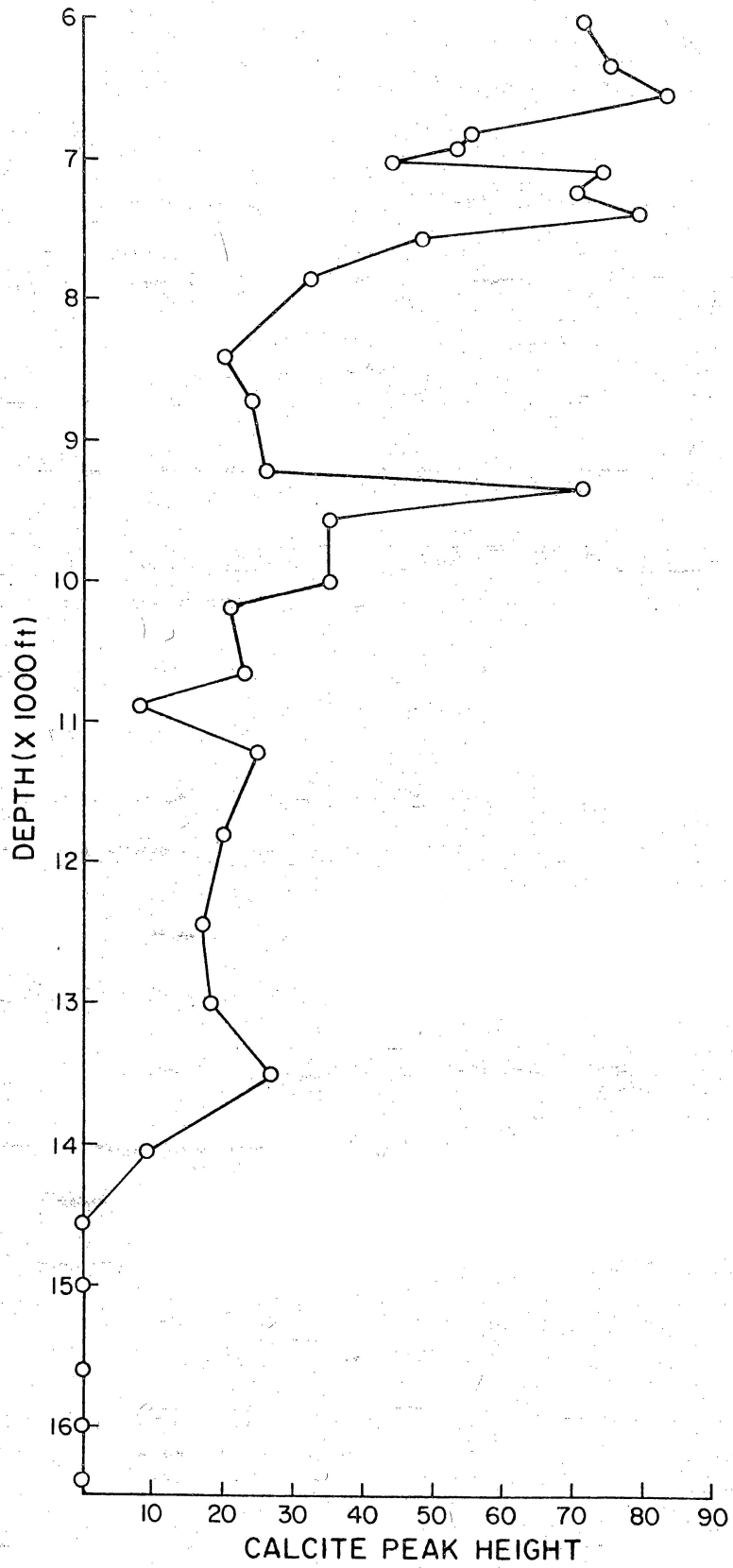


Figure 10. Calcite peaks height from X-ray diffractometer traces versus depth, Brazoria County shales. Hard, splintery shale occurs below 14,000 ft.

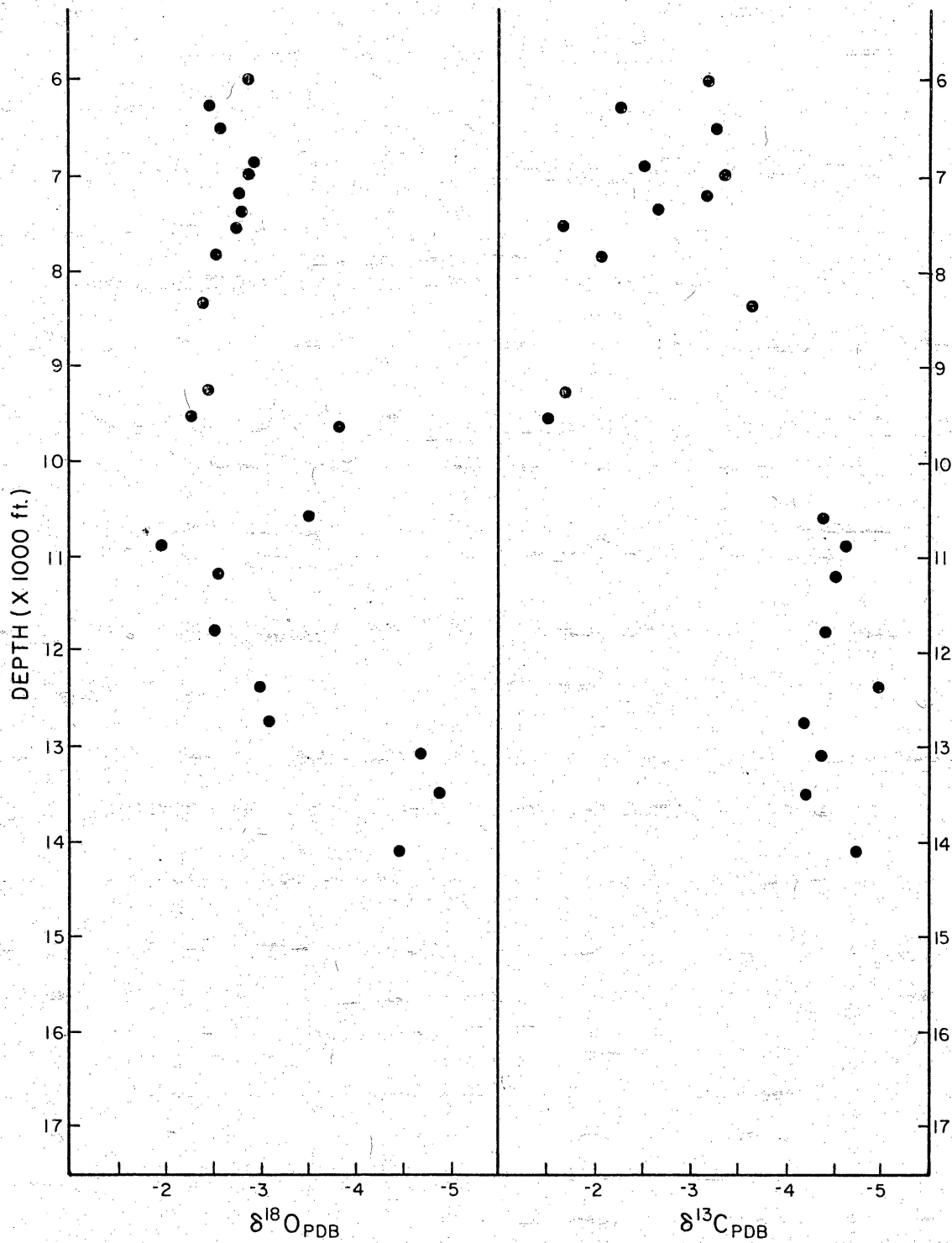


Figure 11. Bulk carbonate oxygen and carbon isotopic data versus depth, Brazoria County shales. No carbonate below 14,000 ft.

Table 1. Brazoria County isotope data.

<u>Well Name</u>	<u>Sample No.</u>	<u>Depth (ft)</u>	$\delta^{18}O$	$\delta^{13}C$
GCO/DOE No. 2 Pleasant Bayou	BrS-1	9,260 - 9,290	-2.44	-1.73
" " " "	BrS-2	9,520 - 9,580	-2.30	-1.59
" " " "	BrS-3	10,010 - 10,040		
" " " "	BrS-4	10,650 - 10,680	-3.54	-4.41
" " " "	BrS-5	11,220 - 11,250	-2.58	-4.54
" " " "	BrS-6	11,800 - 11,840	-2.53	-4.41
" " " "	BrS-7	12,410 - 12,440	-3.02	-4.98
" " " "	BrS-8	13,050 - 13,090	-4.67	-4.38
" " " "	BrS-9	13,510 - 13,540	-4.84	-4.22
" " " "	BrS-10	14,110 - 14,140	-4.46	-4.75
Humble No. 1 Skrabanek	BrS-16	6,874 - 6,906	-2.95	-2.54
" " " "	BrS-17	6,998 - 7,030	-2.89	-3.38
" " " "	BrS-18	7,184 - 7,215	-2.54	-3.18
" " " "	BrS-19	7,336 - 7,367	-2.82	-2.70
" " " "	BrS-20	7,547 - 7,576	-2.77	-1.70
" " " "	BrS-21	7,834 - 7,865	-2.61	-2.11
" " " "	BrS-22	8,361 - 8,393	-2.43	-3.67
" " " "	BrS-23	9,212 - 9,242		
Humble No. 1 Vieman	BrS-24	6,000 - 6,028	-2.905	-3.275
" " " "	BrS-24a	6,000 - 6,028		
" " " "	BrS-25	6,278 - 6,308	-2.49	-2.28
" " " "	BrS-26	6,522 - 6,553	-2.60	-3.28
" " " "	BrS-26a	6,522 - 6,554		
" " " "	BrS-27	6,740 - 6,987		
" " " "	BrS-28	6,987 - 7,019		
GCO/DOE No. 1 Pleasant Bayou	BrS-29	10,240 - 10,260		
" " " "	BrS-30	10,900 - 10,930	-1.99	-4.685
" " " "	BrS-31	12,740 - 12,770	-3.11	-4.20
Humble No. 1 Skrabanek	BrS-32	8,716 - 8,745		

others, 1980) and is consistent with minimal recycling of pore waters between shale and sandstone. In other words, waters were squeezed out of the shales into the sandstones and underwent minor recontact with the shales. Both sandstones and shales shift toward lighter  $\delta^{13}\text{C}$  values at approximately 10,000 ft. The shift in the sandstones, however, is to values of approximately -10 per mil, whereas values in shales below 10,000 ft were approximately -5 per mil. Below approximately 12,500 ft,  $\delta^{13}\text{C}$  values in sandstones become heavier, whereas  $\delta^{13}\text{C}$  values in shales do not show a trend toward heavier values (fig. 11).

Above approximately 10,000 ft,  $\delta^{18}\text{O}$  and  $\delta^{13}\text{C}$  values of shale carbonates are consistent with essentially unmodified skeletal debris. Below this depth isotopic values are still within the range of values possible for skeletal debris but show a trend toward somewhat lighter values with depth. Below approximately 14,000 ft the shales are devoid of carbonate. The shift toward lighter isotopic values below 10,000 ft probably reflects increased amounts of exchange between carbonate particles and shale pore fluids at higher temperature.

## DETRITAL FELDSPAR COMPOSITION

### Background

The Sandstone Consolidation III project includes microprobe analysis of (1) detrital feldspars - to assess the potential consequences of albitization on sandstone diagenesis, and (2) authigenic carbonates - to determine whether any systematic or sequential variations in carbonate chemistry can be documented, and if so, what the implications of such variations are. Because of unforeseen operational problems with and limited access to the University of Texas Geology Department's microprobe, resulting data are limited and preliminary.

We have not yet begun analysis of carbonates but are currently analyzing detrital feldspars from Miocene and Oligocene Frio sandstones from Brazoria County, Texas. On completion of this part of the task, we will conduct similar analyses of feldspars in Vicksburg sandstones from Hidalgo County, Texas, and compare the two data sets. This comparison may tell us if the albitization reaction is dominantly temperature dependent (since upper and lower Texas Gulf coast regions are characterized by differing geothermal gradients) or if other factors are significant controls (for example, whether a "threshold" anorthite content of detrital plagioclase is requisite to albitization; what the potential effect of depositional matrix is on the reaction; and in light of concurrent research on brine chemistry, what the influence of variable pore fluid compositions might be).

#### Sampling and Analytical Techniques

Probe sections were made from whole-core and from hand-picked sandstone cuttings over depth intervals where core was unavailable. This was done to obtain the most continuous depth distribution of samples possible. Ideally, samples were taken every 50 to 100 ft; however, gaps exist owing to the vertical distribution of sandstone in the sedimentary sequence.

Fifty-three polished probe sections were made from Brazoria County samples. Sample depths range from 4,345 ft to 17,783 ft. Acquisition of samples from the lower Texas coast is incomplete. Currently, we have 28 polished sections of Vicksburg sandstones from Hidalgo County.

Microprobe analyses are conducted on an Applied Research Laboratories instrument utilizing an energy dispersive spectrometer. Each section is examined in reflected light, and 20 randomly selected detrital feldspar grains are

analyzed for  $\text{Na}_2\text{O}$ ,  $\text{Al}_2\text{O}_3$ ,  $\text{SiO}_2$ ,  $\text{K}_2\text{O}$ ,  $\text{CaO}$ , and  $\text{FeO}$ . Values of the three feldspar end members, An ( $\text{CaAl}_2\text{Si}_2\text{O}_8$ ), Ab ( $\text{NaAlSi}_3\text{O}_8$ ), and Or ( $\text{KAlSi}_3\text{O}_8$ ) are normalized to 100 percent by the EDS ULTIMATE program. These end member compositions are then plotted on triangular graphs from which potential compositional trends can be readily distinguished.

### Preliminary Results

Two Miocene samples and two Frio samples from the 10,000-ft interval have been analyzed. Preliminary data suggest that the Miocene sandstones and Frio sandstones may have been derived, at least in part, from different sources. On An-Ab-Or plots overprinted with the fields of plutonic/metamorphic and volcanic feldspar compositions (Trevena and Nash, in press), detrital feldspar compositions from the Miocene samples are all consistent with a plutonic/metamorphic source (fig. 12). In contrast, a number of feldspars (fig. 13). While, admittedly, these differences could be attributed to the overlap in the feldspar fields, this seems unlikely. The difference in compositional distributions could be attributed to the overlap of the two genetic fields. There is sufficient overlap to interpret a volcanic as well as a plutonic/metamorphic source for the Miocene samples. However, this seems unlikely; one would expect to find some distinctively volcanic feldspar compositions if a volcanic source were contributing significant sediment during the Miocene.

We had originally proposed to use the feldspar mix of the shallow Miocene samples to establish an initial calcium content to test subsequent changes in feldspar chemistry resulting from progressive burial and albitization. Since we now believe different sediment sources were involved during deposition of the Miocene and the Oligocene Frio sediments, we instead plan to use shallow,

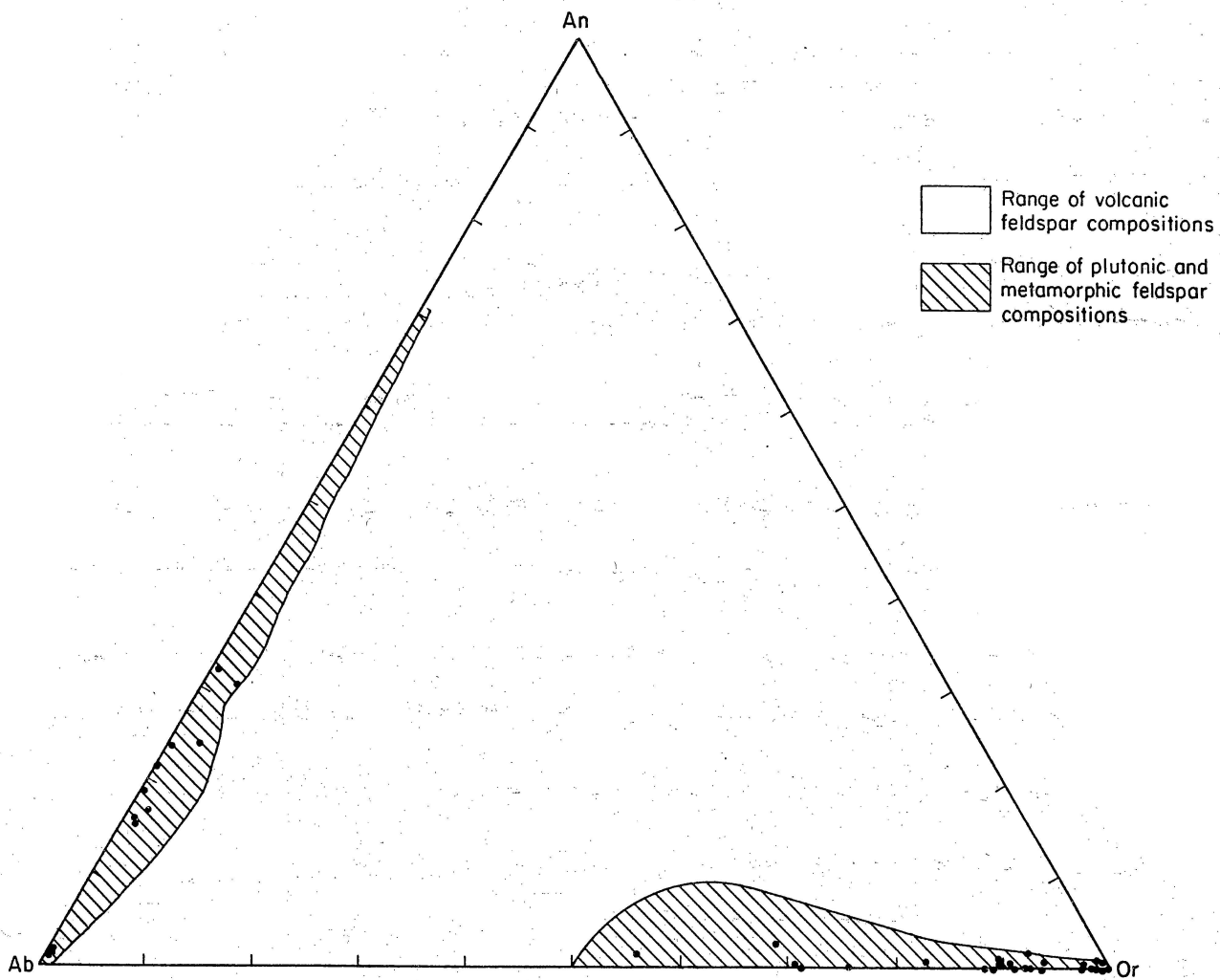


Figure 12. Distribution of detrital feldspar compositions, Miocene (Trevena and Nash, in press).



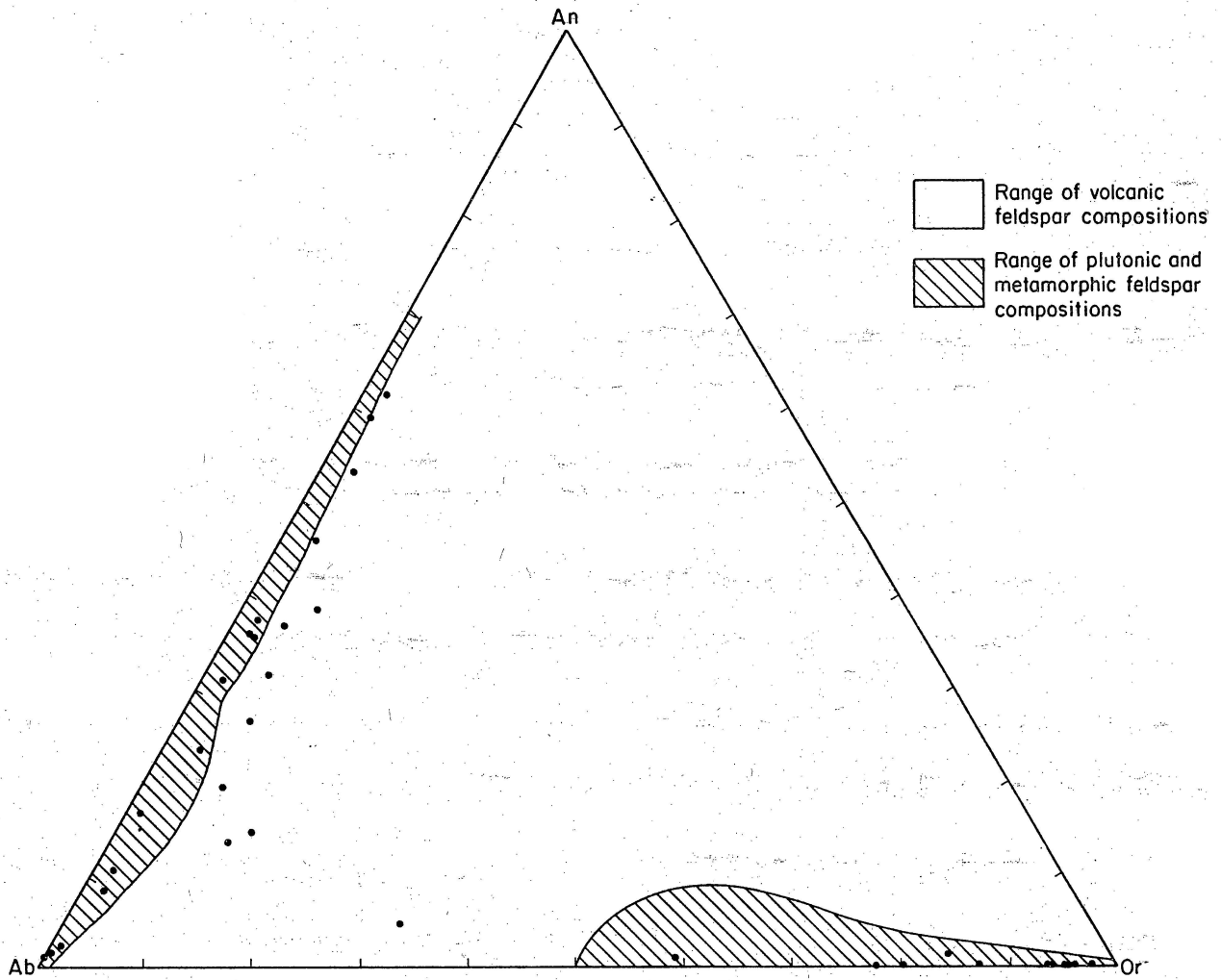


Figure 13. Distribution of detrital feldspar compositions, Frio (10,000 ft interval) (Trevena and Nash, in press).

Frio sandstones poikilotopically cemented with calcite. Our preliminary data suggest that the early poikilotopically cemented sandstones were impermeable to the albitizing fluids. Consequently, in samples having cements that were not leached before burial to depths where albitization occurs, the original feldspar compositions are preserved.

In the Frio samples from the 10,000-ft interval, detrital plagioclase compositions vary from An<sub>1</sub> to An<sub>63</sub> (fig. 13). This range is considerably greater than expected and could complicate determination of a meaningful average initial calcium content if the feldspar compositions have a large standard deviation.

#### ESTIMATING THERMODYNAMIC FUNCTIONS

Thermodynamic data are directly available for construction of many stability diagrams of fair to excellent validity at 25°C (298.15°K). To calculate stability relations among minerals at higher temperatures, between 25 and 200°C, requires data at the temperature of interest. Ideally, tables of the change in standard free energies of formation ( $\Delta G^\circ_f$ ) would be available at higher temperatures in intervals convenient for interpolation. But, because of the fragmentary nature and the lack of availability of thermodynamic data, no comprehensive compilation has been made, especially for the phyllosilicates or layer silicates. However, enough data has been published to allow estimation of  $\Delta G^\circ_f$  for key minerals (table 2) and reactions in tables 3 and 4. The approach is eclectic and is illustrated by calculation of the change in free energies of formation for Ca-montmorillonite and ferroan calcite (table 2).

Table 2. Compositions of key minerals.

1. Quartz	$\text{SiO}_2$
2. Calcite	$\text{CaCO}_3$
3. Ferroan calcite	$\text{Ca}_{.95}\text{Fe}_{.05}\text{CO}_3$
4. Albite	$\text{NaAlSi}_3\text{O}_8$
5. K-feldspar	$\text{KAlSi}_3\text{O}_8$
6. Intermediate plagioclase	$\text{Na}_{.7}\text{Ca}_{.3}\text{Al}_{1.3}\text{Si}_{2.7}\text{O}_8$
7. Kaolinite	$\text{Al}_2\text{Si}_2\text{O}_5(\text{OH})_4$
8. Chlorite	$\text{Mg}_{2.3}\text{Fe}_{2.3}\text{Al}_{2.8}\text{Si}_{2.6}\text{O}_{10}(\text{OH})_8$
9. Ca-montmorillonite	$\text{Ca}_{.16}(\text{Al}_{1.56}\text{Mg}_{.25}\text{Fe}_{.25})\text{Si}_4\text{O}_{10}(\text{OH})_2$
10. Na-montmorillonite	$\text{Na}_{.33}(\text{Al}_{1.56}\text{Mg}_{.25}\text{Fe}_{.25})\text{Si}_4\text{O}_{10}(\text{OH})_2$
11. Illite	$\text{K}_{.6}\text{Mg}_{.25}\text{Al}_{2.3}\text{Si}_{3.5}\text{O}_{10}(\text{OH})_2$
12. Laumontite	$\text{CaAl}_2\text{Si}_4\text{O}_{12} \cdot 4\text{H}_2\text{O}$
13. Clinoptilolite	$\text{NaAlSi}_5\text{O}_{12} \cdot 4\text{H}_2\text{O}$
14. Sphene	$\text{Ca}(\text{Ti}_{.7}\text{Al}_{.4})\text{SiO}_5$

Table 3. Hydrolysis reactions.

1.  $\text{SiO}_2 + 2 \text{H}_2\text{O} = \text{H}_4\text{SiO}_4^\circ$
2.  $\text{CaCO}_3 = \text{Ca}^{2+} + \text{CO}_3^{2-}$
3.  $\text{Ca}_{.95}\text{Fe}_{.05}\text{CO}_3 = 0.95 \text{Ca}^{2+} + 0.05 \text{Fe}^{2+} + \text{CO}_3^{2-}$
4.  $\text{NaAlSi}_3\text{O}_8 + 8 \text{H}_2\text{O} = \text{Na}^+ + \text{Al}(\text{OH})_4^- + 3 \text{H}_4\text{SiO}_4^\circ$
5.  $\text{KAlSi}_3\text{O}_8 + 8 \text{H}_2\text{O} = \text{K}^+ + \text{Al}(\text{OH})_4^- + 3 \text{H}_4\text{SiO}_4^\circ$
6.  $\text{Na}_{.7}\text{Ca}_{.3}\text{Al}_{1.3}\text{Si}_{2.7}\text{O}_8 + 8 \text{H}_2\text{O} = 0.7 \text{Na}^+ + 0.3 \text{Ca}^{2+} + 1.3 \text{Al}(\text{OH})_4^- + 2.7 \text{H}_4\text{SiO}_4^\circ$
7.  $\text{Al}_2\text{Si}_2\text{O}_5(\text{OH})_4 + 7 \text{H}_2\text{O} = 2 \text{Al}(\text{OH})_4^- + 2 \text{H}_4\text{SiO}_4^\circ + 2 \text{H}^+$
8.  $\text{Mg}_{2.3}\text{Fe}_{2.3}\text{Al}_{2.8}\text{Si}_{2.6}\text{O}_{10}(\text{OH})_8 + 3.6 \text{H}_2\text{O} + 6.4 \text{H}^+ = 2.3 \text{Mg}^{2+} + 2.3 \text{Fe}^{2+} + 2.8 \text{Al}(\text{OH})_4^- + 2.6 \text{H}_4\text{SiO}_4^\circ$
9.  $\text{Ca}_{.16}(\text{Al}_{1.56}\text{Mg}_{.25}\text{Fe}_{.25})\text{Si}_4\text{O}_{10}(\text{OH})_2 + 10.24 \text{H}_2\text{O} = 0.16 \text{Ca}^{2+} + 1.56 \text{Al}(\text{OH})_4^- + 0.25 \text{Fe}^{2+} + 0.25 \text{Mg}^{2+} + 4 \text{H}_4\text{SiO}_4^\circ + 0.24 \text{H}^+$
10.  $\text{Na}_{.33}(\text{Al}_{1.56}\text{Mg}_{.25}\text{Fe}_{.25})\text{Si}_4\text{O}_{10}(\text{OH})_2 + 10.24 \text{H}_2\text{O} = 0.33 \text{Na}^+ + 1.56 \text{Al}(\text{OH})_4^- + 0.25 \text{Mg}^{2+} + 0.25 \text{Fe}^{2+} + 4 \text{H}_4\text{SiO}_4^\circ + 0.24 \text{H}^+$
11.  $\text{K}_{.6}\text{Mg}_{.25}\text{Al}_{2.3}\text{Si}_{3.5}\text{O}_{10}(\text{OH})_2 + 11.2 \text{H}_2\text{O} = 0.6 \text{K}^+ + 2.3 \text{Al}(\text{OH})_4^- + 3.5 \text{H}_4\text{SiO}_4^\circ + 0.25 \text{Mg}^{2+} + 1.2 \text{H}^+$
12.  $\text{CaAl}_2\text{Si}_4\text{O}_{12} \cdot 4 \text{H}_2\text{O} + 8 \text{H}_2\text{O} = \text{Ca}^{2+} + 2 \text{Al}(\text{OH})_4^- + 4 \text{H}_4\text{SiO}_4^\circ$
13.  $\text{NaAlSi}_5\text{O}_{12} \cdot 4 \text{H}_2\text{O} + 8 \text{H}_2\text{O} = \text{Na}^+ + \text{Al}(\text{OH})_4^- + 5 \text{H}_4\text{SiO}_4^\circ$
14.  $\text{Ca}(\text{Ti}_{.7}\text{Al}_{.4})\text{SiO}_5 + 2 \text{H}_2\text{O} + 2.3 \text{H}^+ = \text{Ca}^{2+} + 0.7 \text{TiOOH}^+ + 0.4 \text{Al}(\text{OH})_4^- + \text{H}_4\text{SiO}_4^\circ$

Table 4. Reaction pairs.

1.  $\text{CaCO}_3 + 0.05 \text{Fe}^{2+} = \text{Ca}_{.95}\text{Fe}_{.05}\text{CO}_3 + 0.05 \text{Ca}^{2+}$
2.  $2 \text{KAlSi}_3\text{O}_8 + 2 \text{H}^+ + 9 \text{H}_2\text{O} = \text{Al}_2\text{Si}_2\text{O}_5(\text{OH})_4 + 2 \text{K}^+ + 4 \text{H}_4\text{SiO}_4^\circ$
3.  $\text{KAlSi}_3\text{O}_8 + \text{Na}^+ = \text{NaAlSi}_3\text{O}_8 + \text{K}^+$
4.  $\text{Na}_{.7}\text{Ca}_{.3}\text{Al}_{1.3}\text{Si}_{2.7}\text{O}_8 + 0.6 \text{Na}^+ + 1.2 \text{H}_4\text{SiO}_4^\circ = 1.3 \text{NaAlSi}_3\text{O}_8 + 0.3 \text{Ca}^{2+} + 2.4 \text{H}_2\text{O}$
5.  $\text{Na}_{.7}\text{Ca}_{.3}\text{Al}_{1.3}\text{Si}_{2.7}\text{O}_8 + 1.3 \text{H}^+ + 3.45 \text{H}_2\text{O} = 0.65 \text{Al}_2\text{Si}_2\text{O}_5(\text{OH})_4 + 0.3 \text{Ca}^{2+} + 0.7 \text{Na}^+ + 1.4 \text{H}_4\text{SiO}_4^\circ$
6.  $1.4 \text{Al}_2\text{Si}_2\text{O}_5(\text{OH})_4 + 2.3 \text{Mg}^{2+} + 2.3 \text{Fe}^{2+} + 6.2 \text{H}_2\text{O} = \text{Mg}_{2.3}\text{Fe}_{2.3}\text{Al}_{2.8}\text{Si}_{2.6}\text{O}_{10}(\text{OH})_8 + 0.2 \text{H}_4\text{SiO}_4^\circ + 9.2 \text{H}^+$
7.  $\text{Ca}_{.16}(\text{Al}_{1.56}\text{Mg}_{.25}\text{Fe}_{.25})\text{Si}_4\text{O}_{10}(\text{OH})_2 + 1.32 \text{H}^+ + 4.78 \text{H}_2\text{O} = 0.78 \text{Al}_2\text{Si}_2\text{O}_5(\text{OH})_4 + 0.25 \text{Mg}^{2+} + 0.25 \text{Fe}^{2+} + 0.16 \text{Ca}^{2+} + 2.44 \text{H}_4\text{SiO}_4^\circ$
8.  $\text{Ca}_{.16}(\text{Al}_{1.56}\text{Mg}_{.25}\text{Fe}_{.25})\text{Si}_4\text{O}_{10}(\text{OH})_2 + 0.41 \text{K}^+ + 0.57 \text{H}^+ + 2.64 \text{H}_2\text{O} =$   
 $0.68 \text{K}_{.6}\text{Mg}_{.25}\text{Al}_{2.3}\text{Si}_{3.5}\text{O}_{10}(\text{OH})_2 + 0.08 \text{Mg}^{2+} + 0.25 \text{Fe}^{2+} + 0.16 \text{Ca}^{2+} + 1.62 \text{H}_4\text{SiO}_4^\circ$
9.  $\text{K}_{.6}\text{Mg}_{.25}\text{Al}_{2.3}\text{Si}_{3.5}\text{O}_{10}(\text{OH})_2 + 1.1 \text{H}^+ + 3.15 \text{H}_2\text{O} = 1.15 \text{Al}_2\text{Si}_2\text{O}_5(\text{OH})_4 + 0.6 \text{K}^+ + 1.2 \text{H}_4\text{SiO}_4^\circ + 0.25 \text{Mg}^{2+}$
10.  $\text{NaAlSi}_5\text{O}_{12} \cdot 4 \text{H}_2\text{O} + \text{Ca}^{2+} + \text{Al}(\text{OH})_4^- = \text{CaAl}_2\text{Si}_4\text{O}_{12} \cdot 4 \text{H}_2\text{O} + \text{Na}^+ + \text{H}_4\text{SiO}_4^\circ$
11.  $\text{CaCO}_3 + 2 \text{Al}(\text{OH})_4^- + 4 \text{H}_4\text{SiO}_4^\circ + 2 \text{H}^+ = \text{CaAl}_2\text{Si}_4\text{O}_{12} \cdot 4 \text{H}_2\text{O} + 8 \text{H}_2\text{O} + \text{H}_2\text{CO}_3^\circ$

Note: All reactions written with Al immobile.

## Ca-Montmorillonite

A method suggested by Helgeson (personal communication, 1971) is used here because it enables estimation of thermodynamic functions at temperatures greater than 25°C. The standard change in enthalpy of formation ( $\Delta H^\circ_f$ ) for Ca-montmorillonite is estimated graphically from a curve derived from phyllosilicates in general (fig. 14). For the ordinate, the change in enthalpy of formation of a particular phyllosilicate is divided by the total number of tetrahedrally coordinated Si and Al atoms ( $Si_{Tet} + Al_{Tet}$ ). The values along the abscissae are obtained by considering octahedral and exchangeable ionic constituents and hydroxyl ions. The enthalpies of formation of these species in aqueous solution, multiplied by their respective stoichiometric coefficients, are summed and divided by ( $Si_{Tet} + Al_{Tet}$ ). A surprisingly good fit for all available phyllosilicate data can be made with a straight line. The standard change in entropy ( $\Delta S^\circ_f$ ) is calculated from the relationship,  $S^\circ_{abs} - S^\circ_f = \Delta S^\circ_f$ . Absolute entropy ( $S^\circ_{abs}$ ) is estimated by summing the oxide constituents where water is treated as ice. The entropy of formation ( $S^\circ_f$ ) is calculated by summing elemental entropies. Accordingly,  $\Delta H^\circ_f$  and  $\Delta S^\circ_f$  at 25°C for Ca-montmorillonite are -1352 kcal/mole and -294 cal/degmole, respectively. Thus,  $\Delta G^\circ_f$  is -1264.4 kcal/mole at 25°C from the relationship,  $\Delta G^\circ_f = \Delta H^\circ_f - T\Delta S^\circ_f$ . Using a method suggested by Tardy and Garrels (1974),  $\Delta G^\circ_f$  at 25°C is estimated at -1257.2 kcal/mole. Enthalpies can be calculated at higher temperatures using average heat capacity data (Helgeson, 1969) to prepare curves for the appropriate temperature (fig. 14). Values of entropies for oxides and elements at higher temperatures can be interpolated from Robie and others (1978).

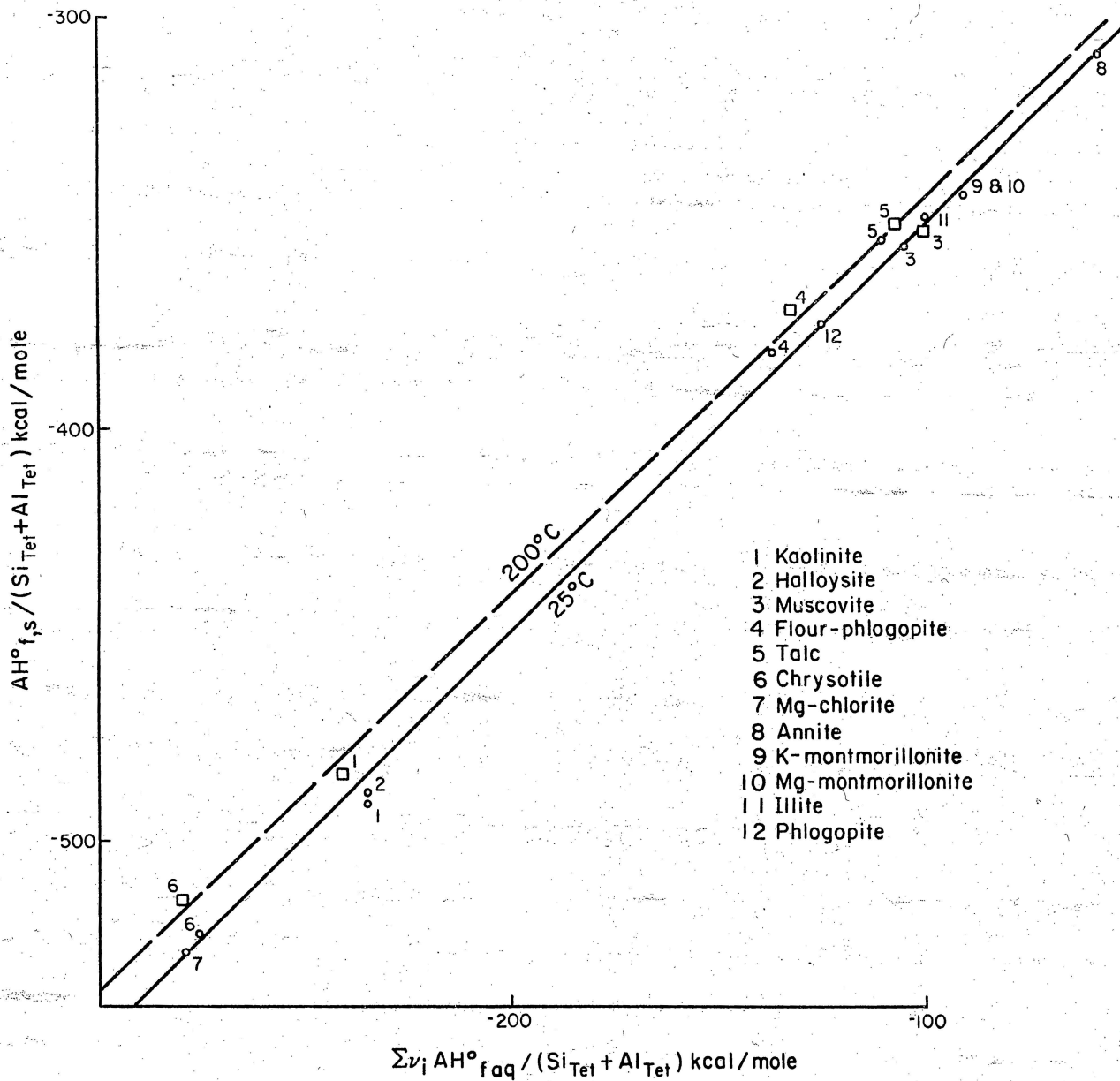


Figure 14. Estimation of the standard change in enthalpy of formation of phyllosilicates. Circles are data points at 25°C, squares data points at 200°C.

## Ferroan Calcite

The calculation of  $\Delta G^\circ_f$  for ferroan calcite (and intermediate plagioclase) (table 2) is essentially the estimation of  $\Delta G^\circ_f$  for solid solutions. Ferroan calcite is considered a mixture in which calcite and siderite are pure end members. For solid solution,

$$\Delta G^\circ_f = X_1 \Delta G^\circ_{f,1} + X_2 \Delta G^\circ_{f,2} + RT (X_1 \ln X_1 + X_2 \ln X_2)$$

where  $X_1$  and  $X_2$  are the mole fractions of component 1 and 2, respectively, and  $\Delta G^\circ_{f,1}$  and  $\Delta G^\circ_{f,2}$  are the standard change in free energies of formation for components 1 and 2, in this case calcite and siderite. To illustrate the method,  $\log K_r$  is calculated for the reaction,  $\text{Ca}_{.95}\text{Fe}_{.05}\text{CO}_3 = .95 \text{Ca}^{2+} + .05 \text{Fe}^{2+} + \text{CO}_3^{2-}$ . Calculation of  $\Delta G^\circ_f$  at 25°C according to

$$\Delta G^\circ_f = X_{\text{CaCO}_3} \Delta G^\circ_{f\text{CaCO}_3} + X_{\text{FeCO}_3} \Delta G^\circ_{f\text{FeCO}_3} + RT (X_{\text{CaCO}_3} \ln X_{\text{CaCO}_3} + X_{\text{FeCO}_3} \ln X_{\text{FeCO}_3}),$$

substituting free energy values and mole fractions, yields a  $\Delta G^\circ_f = -264.4$  kcal/mole. This value is almost identical to a value of  $-264.3$  kcal/mole obtained using an alternative method (Boles, 1978).  $\Delta G^\circ_r$  is then  $+11.59$  kcal/mole and therefore  $\log K_r$  is  $-8.50$ .

To estimate  $\Delta G^\circ_r$  at higher temperatures requires calculation of  $\Delta H^\circ_r$ .  $\Delta S^\circ_f = -62.53$  cal/degmole, since  $S^\circ_{\text{abs}}$  of ferroan calcite calculated from the oxides is  $22.17$  cal/degmole, and  $S^\circ_f$  from the elements is  $84.70$  cal/degmole. For ferroan calcite  $\Delta H^\circ_f = -283.03$  kcal/mole, from the relationship  $\Delta H^\circ_f = \Delta G^\circ_f + T\Delta S^\circ_f$ , and therefore  $\Delta H^\circ_r$  at 25°C is  $-2.91$  kcal/mole. Assuming  $\Delta H^\circ_r$  is



constant over the temperature range of 25 to 200°C, log  $K_r$  can be easily calculated from the Van't Hoff equation:

$$\log K_T = - \frac{\Delta H^\circ_r}{2.303R} \left( \frac{1}{T} - \frac{1}{298} \right) + \log K_{298}$$

to establish relative solubilities of ferroan calcite and calcite where T is in degrees Kelvin. Under these assumptions log  $K_r$  at 100°C is -8.95 for ferroan calcite and -8.73 for calcite.

Thermodynamically, calcite at pH less than about 8 is more soluble than ferroan calcite. Solutions with a  $\text{Ca}^{2+}/\text{Fe}^{2+}$  ratio less than 1.41 will first yield ferroan calcite. Predictably, then in shales, authigenic iron-bearing carbonate would be favored, since the smectite/illite transformation (table 4) yields a  $\text{Ca}^{2+}/\text{Fe}^{2+}$  ratio of 0.64. Indeed, energy dispersive analysis shows authigenic carbonate to be iron bearing (fig. 9).

#### ACKNOWLEDGMENTS

This research was supported by the U.S. Department of Energy under contract number DE-AC08-79ET27111. Figures were drafted under the direction of James W. Macon, Chief Cartographer.

## REFERENCES

- Boles, J. R., 1978, Active ankerite cementation in the subsurface Eocene of southwest Texas: *Contributions to Mineralogy and Petrology*, v. 68, p. 13-22.
- Freed, R. L., 1980, Shale mineralogy and burial diagenesis in four geopressured wells, Hidalgo and Brazoria Counties, Texas, in Loucks, R. G., Richmann, D. L., and Milliken, K. L., Factors controlling reservoir quality in Tertiary sandstones and their significance to geopressured geothermal production: U.S. Department of Energy, Division of Geothermal Energy Report DOE/ET/27111-1, Appendix A, p. 111-172.
- Helgeson, H. C., 1969, Thermodynamics of hydrothermal systems at elevated temperatures and pressures: *American Journal of Science*, v. 267, p. 729-804.
- Loucks, R. G., Richmann, D. L., and Milliken, K. L. 1980, Factors controlling reservoir quality in Tertiary sandstones and their significance to geopressured geothermal production: U.S. Department of Energy, Division of Geothermal Energy Report DOE/ET/27111-1, 188 p.
- Robie, R. A., Hemingway, B. S., and Fisher, J. R., 1978, Thermodynamic properties of minerals and related substances at 298.15K and 1 bar ( $10^5$  Pascals) pressure and at higher temperatures: U.S. Geological Survey Bulletin 1452, 456 p.
- Tardy, Y., and Garrels, R. M., 1974, A method of estimating the Gibbs energies of formation of layer silicates: *Geochimica et Cosmochimica Acta*, v. 38, p. 1101-1116.
- Trevena, A. S., and Nash, W. P., in press, An electron microprobe study of detrital feldspar: *Journal of Sedimentary Petrology*.